# Three-dimensional bonded-cell model for grain fragmentation

David Cantor Garcia, Émilien Azéma, Philippe Sornay, Farhang Radjai

# Three-dimensional bonded-cell model for grain fragmentation

**D. Cantor**[1,2] · **E. Azéma**[1,3] · **P. Sornay**[2] · **F. Radjai**[1,4]

**Abstract** We present a three-dimensional numerical method for the simulation of particle crushing in 3D. This model is capable of producing irregular angular fragments upon particle fragmentation while conserving the total volume. The particle is modeled as a cluster of rigid polyhedral cells generated by a Voronoi tessellation. The cells are bonded along their faces by a cohesive Tresca law with independent tensile and shear strengths and simulated by the contact dynamics method. Using this model, we analyze the mechanical response of a single particle subjected to diametral compression for varying number of cells, their degree of disorder, and intercell tensile and shear strength. In particular, we identify the functional dependence of particle strength on the intercell strengths. We find that two different regimes can be distinguished depending on whether intercell shear strength is below or above its tensile strength. In both regimes, we observe a power-law dependence of particle strength on both intercell strengths but with different exponents. The strong effect of intercell shear strength on the particle strength reflects an interlocking effect between cells. In fact, even at low tensile strength, the particle global strength can still considerably increase with intercell shear strength. We finally show that the Weibull statistics describes well the particle strength variability.

**Keywords** Bonded-cell model · Fragmentation · Discrete element method · Contact dynamics method · Voronoi cell · Weibull statistics

✉ D. Cantor
david.cantor@umontpellier.fr

[1] Laboratoire de Mécanique et Génie Civil (LMGC), Université de Montpellier, CNRS, Montpellier, France

[2] CEA, DEN, DEC, SFER, LCU, 13108 Saint Paul lez Durance, France

[3] Department of Mechanical Engineering, Faculty of Engineering, Chiang Mai University, 239 Huay Kaew Rd, Chiang Mai 50200, Thailand

[4] Multi-Scale Materials Science for Energy and Environment <MSE>$^2$, UMI 3466 CNRS-MIT Energy Initiative, Massachusetts Institute of Technology, 77 Massachusetts Avenue, Cambridge, MA 02139, USA

## 1 Introduction

The fragmentation of particles is an important factor in everyday use of granular materials and in processing industries dealing with powders and grains. It modifies the grain size distribution [9,21,33], packing fraction [15,25,29], shear strength [30], yielding surface [34,50], and microstructure of granular materials [31]. However, there is presently no clear quantitative understanding of such effects in the rheology and processing of granular materials and, conversely, the properties of the fragments such as their size, shape, and strengths cannot be predicted from the process [23].

The effects of particle crushing can be investigated experimentally but its origins are much more difficult to trace back to the particle scale. In a similar vein, some continuum mechanics models are able to reproduce phenomenologically the effects of particle fragmentation or degradation [8,13]. Such models are, however, mostly based on idealized description of grain failure. For these reasons, numerical simulations based on the discrete element method (DEM) have been extensively used for a better understanding of the fragmentation process and its impact on the macroscopic behavior. The first DEM simulations of crushable particles were proposed in the late 80s [62] and 90s [1,28,58]. Initially, these models were two-dimensional and involved simplified (circular) shapes of fragments and their interactions (frictional con-

tacts). 2D simulations are now capable of reproducing the evolution of cracks and complex geometries of fragments [39,40].

With increasing computational power, three-dimensional models have also been introduced recently. These models can be classified at least in two main groups. The first group, which we call *Replacing Method*, consists in substituting each broken particle when typically a load threshold is reached by a set of smaller particles [16,61]. However, a nonconservation of mass and volume may occur as the replacements are made and artificial overlapping between particles is sometimes allowed, producing local elastic overstresses.

The second group, which was coined *Bonded-Cell Method* (BCM) in Ref. [40], is based on the construction of particles by agglomerating a set of potential fragments. These small fragments are held together by diverse mechanisms that assign a bonding strength at each contact. The bonding of spheres is the most wide-spread model to simulate crushing in 3D. However, the spheres are obviously unable to reproduce the broad shape variability of fragments. Moreover, the apparent volume of a sphere agglomerate is considerably larger than those of its fragments. In order to circumvent these problems, some authors have used polygonal or polyhedral subparticles or cells generated by Voronoi tessellation [22]. These cells pave the whole volume of the particle so that the volume is conserved during particle fracture and fragmentation. Nevertheless, intercell contacts are modeled by a linear force law as that between spherical subparticles. This is clearly an unphysical approximation since the contacts extend along a surface between cells and a realistic model must account for the fact that the treatment of such contacts need at least three displacement variables at three independent contact points.

In this paper, we introduce a three-dimensional BCM approach in the framework of the contact dynamics (CD) method. In 3D, each particle is composed of cells of irregular polyhedral shape. The framework of the CD method has the advantage of accounting for the correct kinematics of face–face contacts between fragments [27,46]. Furthermore, the treatment of cells as rigid particles leads to numerically efficient simulations in 3D. We also introduce a general cohesive law governing cell interactions before fracture. Using this approach, we investigate the fracture properties of a single particle subjected to diametral compression.

This paper is organized as follows: In Sect. 2.3, we present the 3D BCM as well as the treatment of intercell contacts within the CD method. In Sect. 3, numerical simulations of diametral compaction are introduced. In Sect. 3.2, we investigate the effects of different geometrical and mechanical parameters on the particle strength. Finally, in Sect. 4, a brief summary and perspectives of this work are presented.

## 2 BCM with contact dynamics

### 2.1 Voronoi meshing

We perform a three-dimensional meshing of polyhedral particles with the help of the package NEPER [43] and using a centroidal Voronoi tessellation [18]. In general, a Voronoi tessellation is a division of a space $\mathbf{X}$ in $\mathbb{R}^N$ via a set of points or generators $\{P_j\}$. The main property of this division is that any point $x$ belongs to a Voronoi cell $V_i$ if a distance function $d(x, P_i)$ is minimal between all the generators [42]. A compact definition of a Voronoi cell may be written as follows:

$$V_i = \{x \in \mathbf{X} \mid d(x, P_i) < d(x, P_j)\ \forall\ j \neq i\}. \tag{1}$$

In three dimensions, the Voronoi tessellation produces always convex polyhedra sharing common faces if the region $\mathbf{X}$ is also convex.

Furthermore, a centroidal Voronoi tessellation has the property that the generators are also the centroids of the cells. The points $\{P_j\}$ are usually located randomly and, as a consequence, the locations of those points differ from those of the corresponding cell centroids $\{c_j\}$. One possible technique to reduce the distances $d(P_j, c_j)$ is known as the Lloyd's method. This iterative procedure may be described as follows:

1. Define the space $\mathbf{X}$,
2. select points $\{P_j\}$,
3. define the corresponding cells $\{V_j\}$,
4. compute the centroid of each cell $\{c_j\}$,
5. replace points $\{P_j\}$ with points $\{c_j\}$ and recompute $\{V_j\}$,
6. repeat from step 4 until a convergence criterion is satisfied.

The convergence criterion that is used in this work may be written as follows:

$$\frac{\sum_{j=1}^{n_{\mathrm{cl}}} d(P_j, c_j)}{\sum_{j=1}^{n_{\mathrm{cl}}} r_j} \leq \lambda, \tag{2}$$

where $n_{\mathrm{cl}}$ is the number of cells, and $r_j$ is the average radius of cell $j$. This ratio should be below or equal the tolerance $\lambda$ at which we stop the iterations. The quantity $\lambda$ is actually a quite interesting parameter because, as it is shown below, it may be interpreted as a measure of disorder of the cell shapes and their distributions.

Figures 1 and 2 display several examples of meshing of a truncated icosahedron, a semiregular polyhedron with 60 vertices and 21 faces, for $\lambda = 0.25$ and two different numbers of cells, and for $n_{\mathrm{cl}} = 250$ and two values of $\lambda$, respectively. In general, values of $\lambda \simeq 0$ produce less elongated shapes and

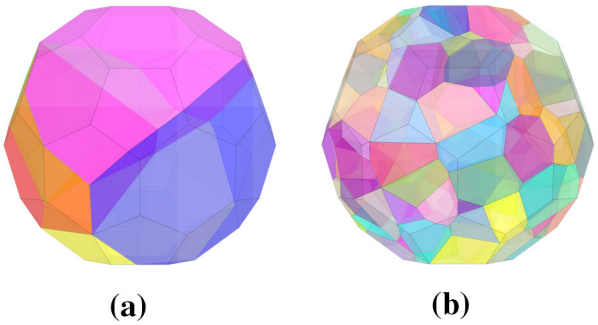


**Fig. 1** Examples of icosahedral particles for $\lambda = 0.25$ and meshed by **a** 5 and **b** 250 cells

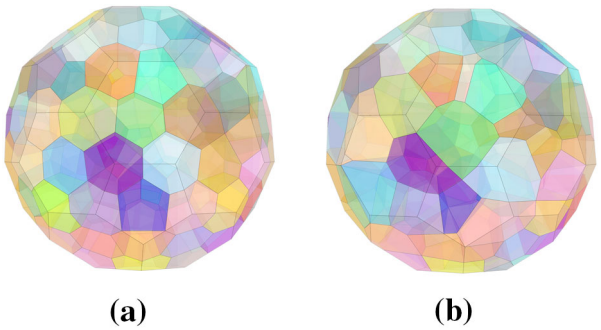


**Fig. 2** Examples of icosahedral particles composed of 250 Voronoi cells and disorder parameters $\lambda = 0.005$ (**a**) and $\lambda = 0.5$ (**b**)

the cells are well distributed in the volume. As $\lambda$ increases, the dislocation of the centroids with respect to the generators create disorder in the assembly of cells.

By construction, the sizes of the initial aggregates and cells determine the upper and lower bounds of the fragment size distributions during crushing simulations. In this sense, for DEM simulations it is important to optimize the number of cells per aggregate in order to ensure the representativity of the fragments sizes for a convenient computational time.

### 2.2 Cell interactions

The contact between two polyhedral shapes can have three different geometries: contact point, contact line, and contact surface, as shown schematically in Fig. 3. The determination of the contacts between two polyhedral cells is performed in several steps. First, a "bounding box" method is used to compute a list of neighboring pairs. Then, for each pair, the overlaps are calculated through the so-called "common plane" method introduced by Cundall [17]. This is an iterative method based on the perturbation of the orientation of the normal vector. The process is initialized by a first guess based on the vector joining the centers of the two polyhedra. This detection procedure is fairly rapid when correctly optimized [37,38]. The interactions may include

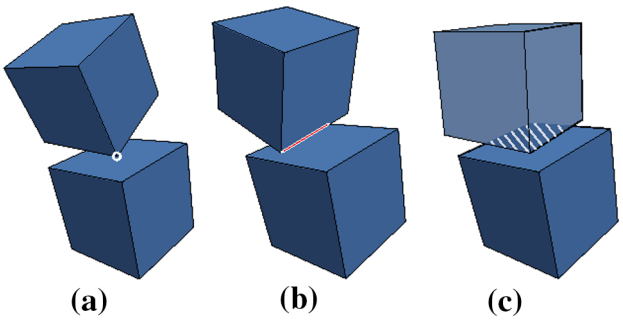


**Fig. 3** Examples of contact types that may occur between polyhedral cells: **a** Point, **b** line, and **c** surface

vertex–vertex, vertex–edge, vertex–face, edge–edge, edge–face, or face–face contacts. The contact line, such as that produced by a edge–face interaction, can be represented by two distinct points, whereas a surface (face–face) contact can be replaced by three points since they involve an equivalent number of geometrical unilateral constraints between two faces. Note that vertex–vertex or vertex–edge contacts are rare but, when they occur, the common plane method is able to provide a normal direction based on geometrical criteria.

In the Bonded-Cell Method, we assume that rigid cells interact only via cohesive forces through face–face contacts. The normal adhesion threshold $f_n^c$ depends on the area $S$ of the contact. Since the contact plane is represented by three points, the tensile threshold for each contact point is given by $f_n^c = C_n S/3$, where $C_n$ is the internal cohesion of the material. In the same way, the shear threshold for each contact point in the contact plane is given by $f_t^c = C_t S/3$, where $C_t$ is the contact shear strength. $C_n$ and $C_t$ are assumed to be independent strength parameters of the material. Once either of the critical stresses is reached, the intercell bond breaks irreversibly and the interaction turns into a frictional contact with coefficient of friction $\mu_{cl}$. Note that, since the cells are rigid, a cohesive face–face contact can not kinematically break until the three points representing the interface do so, i.e., when either of the two thresholds is reached for each of the three points.

The normal force $f_n$ and normal velocity $u_n$ at each contact point satisfy the following relations [46]

$$\begin{cases} u_n > 0 \Rightarrow f_n = 0 \\ u_n = 0 \Rightarrow f_n + C_n S/3 > 0 \end{cases} \tag{3}$$

which simply expresses the unilateral nature of the contact between the two cells at their contact points in the presence of a cohesive force. In the same way, along the tangential direction, we have the following relation between the tangential force $f_t$ and the tangential velocity $u_t$:

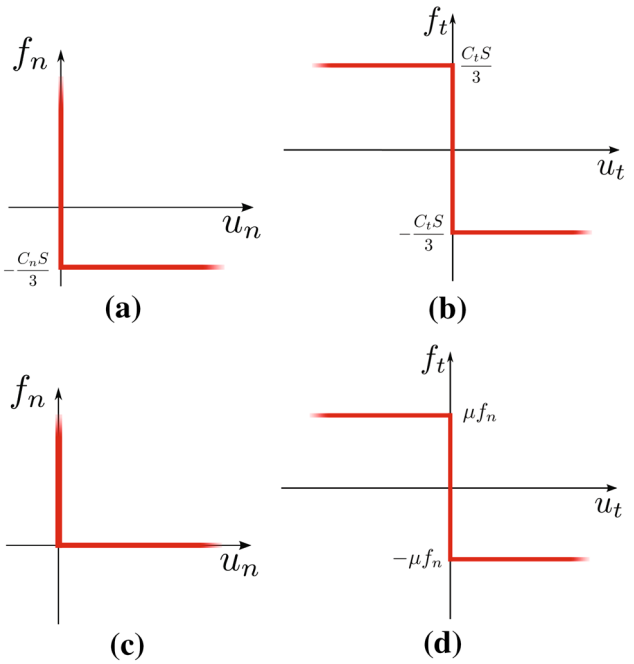


**Fig. 4** Complementarity relations along the normal and tangential directions of the contact frame for cohesive contacts (**a**, **b**) and broken contacts (**c**, **d**) respectively

$$\begin{cases} u_t > 0 \Rightarrow f_t = -C_t S/3 \\ u_t = 0 \Rightarrow -C_t S/3 \le f_t \le C_t S/3 \\ u_t < 0 \Rightarrow f_t = C_t S/3 \end{cases} . \tag{4}$$

These "complementarity relations" are represented by two graphs shown in Fig. 4a, b.

The above relations should be taken into account together with the equations of motion in order to determine both the velocities and forces at all contacts in the system. We use the contact dynamics (CD) method, which, as briefly discussed below, allows for exact prescription of these relations based on an implicit time-stepping integration scheme. To use molecular dynamics (MD) or common DEM, it is necessary to regularize the above relations so that the classical explicit integration schemes can be applied.

At each time step, the "critical" contact points, where $u_n > 0$ (separation) or $|u_t| > 0$ (sliding), break irreversibly and the contact point turns into a cohesionless frictional contact governed by the following relations:

$$\begin{cases} u_n > 0 \Rightarrow f_n = 0 \\ u_n = 0 \Rightarrow f_n > 0 \end{cases} \tag{5}$$

and

$$\begin{cases} u_t > 0 \Rightarrow f_t = -\mu_{\mathrm{cl}} f_n \\ u_t = 0 \Rightarrow -\mu_{\mathrm{cl}} f_n \le f_t \le \mu_{\mathrm{cl}} f_n \\ u_t < 0 \Rightarrow f_t = \mu_{\mathrm{cl}} f_n \end{cases} . \tag{6}$$

The graphs of these relations are shown in Fig. 4c, d.

### 2.3 Contact dynamics

The above complementarity relations were prescribed within the CD method [27,35,46,59]. In this method, the rigid-body equations of motion are integrated for all particles, which are treated as undeformable bodies, by taking into account the kinematic constraints resulting from the complementarity relations. An iterative algorithm similar to Gauss–Seidel iterations is used to determine the contact forces and particle velocities simultaneously at all potential contacts. Since this algorithm is implicit, the contact velocities $u_n$ and $u_t$ entering the complementarity relations can represent the velocities $u_n^+$ and $u_t^+$ at the end of a time step. This is equivalent to the assumption that the coefficients $e_n$ and $e_t$ of normal and tangential restitution are both zero. However, it is also possible to use the complementarity relations with the following weighted means:

$$u^n = \frac{e_n u_n^- + u_n^+}{1 + e_n} \tag{7}$$

$$u^t = \frac{e_t u_t^- + u_t^+}{1 + e_t}, \tag{8}$$

where $u_n^-$ and $u_t^-$ are the normal and tangential contact velocities at the beginning of a time step. With complementary relations involving these weighted velocities, it can be shown that in a binary collision between two particles the postcollisional velocities are indeed given by $u_n^+ = -e_n u_n^-$ and $u_t^+ = -e_t u_t^-$. In this way the contact laws involve five independent parameters: coefficient of friction $\mu_{\mathrm{cl}}$, coefficient of normal restitution $e_n$, coefficient of tangential restitution $e_t$, normal cohesive strength $C_n$, and tangential cohesive strength $C_t$.

An implicit time-stepping scheme makes the CD method unconditionally stable. In contrast to the molecular dynamics method, in the CD method the tiny numerical overlaps between particles are used for contact detection but they do not represent an elastic deflection. For this reason, the time step can be larger than that in the MD method or DEM. The CD method has been extensively employed for the simulation of granular materials in 2D and 3D [2,4–7,12,19,36,41,44,45,48,49,51–54,56,57]. We implemented the Bonded-Cell method in the software LMGC90 [20]. Video samples of diametral compression tests can be found at www.cgp-gateway.org/ref035.

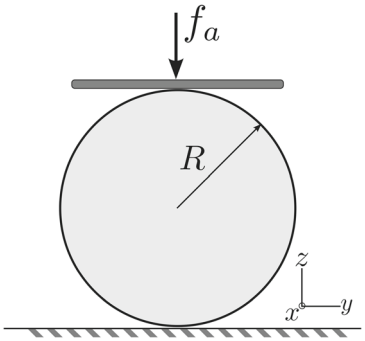


**Fig. 5** Schematic representation of diametral compression test on a particle of average radius $R$

## 3 Diametral compression and particle strength

### 3.1 Diametral compression of an icosahedron

We consider icosahedral particles of mean radius $R$ compressed between two platens, as illustrated in Fig. 5. A gradually increasing vertical force $f^a$ is applied on the top platen. The platens directly touch two opposite hexagonal faces of the icosahedron. Hence, the force $f_a$ is always exerted on this supporting hexagonal surface belonging to the periphery of the particle. This surface may be shared between several cells depending on the number $n_{\mathrm{cl}}$ of cells inside the icosahedron. As $f_a$ is increased from zero, the contact forces inside the particle increase proportionally to $f_a$ but, since the particle is rigid, no fracture occurs until a threshold $f_c$ is reached. At this point, an unstable failure of the particle occurs and the particle breaks into several fragments. Several snapshots of a particle at incipient crushing are shown in Fig. 6. The subsequent fragmentation is a dynamic process and can be investigated under controlled displacement of the top platen. Here we are interested in the initiation of failure and the breaking force $f_c$, which represents the particle strength.

The intercell breaking strengths $C_n$ and $C_t$ having the dimensions of a stress, the particle strength should be expressed as a stress threshold $\sigma_c$. However, the stress field inside a particle subjected to diametral compression is nonuniform [14,60]. The average vertical stress in the largest section of the particle $\pi R^2$ is $f_a/\pi R^2$. The highest tensile stress inside the particle can be much larger than this stress. In our meshed particles, even with a large number of cells, the disordered configuration of the cells results in a strongly inhomogeneous distribution of intercell forces. Figure 7 shows an example of intercell forces in a particle composed of 150 cells. We observe both compressive forces along the vertical direction and tensile forces along the horizontal direction. We can compute the average vertical stress from the forces by applying the following well-known micromechanical expression:

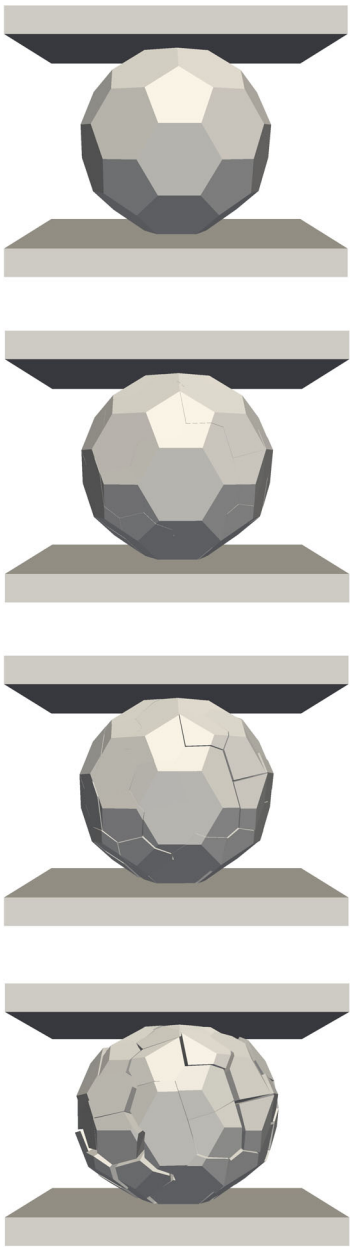

**Fig. 6** Snapshots of a particle composed of 75 cells undergoing incipient breakage under the action of a vertical force

$$\sigma_a = \frac{1}{V}\sum_{\alpha\in V} f_z^\alpha \ell_z^\alpha, \tag{9}$$

where $V$ is the volume of the particle, $\alpha$ denotes the contact labels between the cells, $f_z$ is the vertical component of the intercell force, and $\ell_z$ is the vertical component of the branch vector joining the centers of cells. This average stress is proportional to $f_a/\pi R^2$ by a factor of 1.2 and it reaches its maximum value for $f_c$. Note that, to avoid inhomogeneities induced by gravity, the latter is set to zero although its value is by orders of magnitude below the breaking threshold $f_c$.

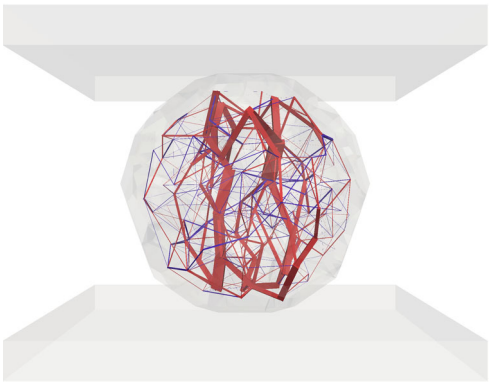

**Fig. 7** Intercell forces in a particle composed of 150 cells subjected to diametral compression. *Line thickness* is proportional to the force. The compressive and tensile forces are in *red* and *blue*, respectively

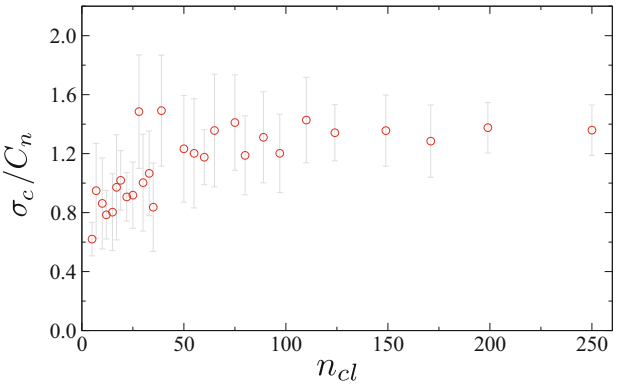


**Fig. 8** Evolution of particle strength with the number of cells. Each point represents an average value over 10 independent cell configurations. The *error bars* represent minimum and maximum values

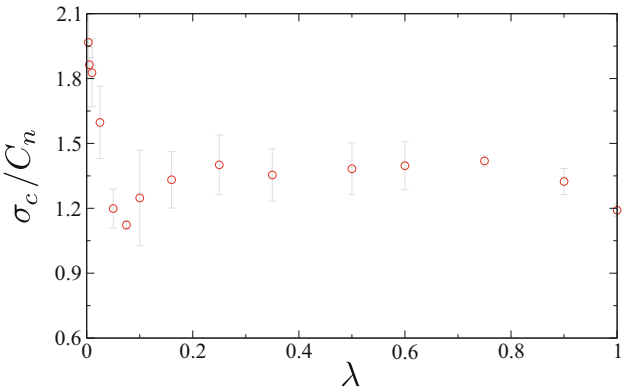


**Fig. 9** Evolution of particle strength as a function of the degree of disorder

### 3.2 Effects of meshing on the particle strength

We performed a series of simulations with a particle of constant size but varying number $n_{\mathrm{cl}}$ of cells and degree of disorder $\lambda$. In these simulations, the intercell strengths are kept constant and equal $C_n = C_t$. The intercell coefficient of friction, which becomes effective only when an intercell contact fails, is set to $\mu_{cl} = 0.4$. Figure 8 shows the vertical strength $\sigma_c$, normalized by normal strength $C_n$, as a function of $n_{\mathrm{cl}}$. Each point represents the mean value for 10 simulations performed with particles composed of cells with the same degree of disorder $\lambda = 0.25$ and the same strength, but independent Voronoi tessellations for the generation of the cells. The maximum and minimum values are shown by error bars.

Despite the large variability of the data, specially at small numbers of cells, we see that the particle strength increases on the average with $n_{\mathrm{cl}}$ and it becomes independent of it beyond 75 cells. We also observe that this steady value of the particle strength is nearly 1.25 times the intercell strength $C_n$. The high variability of the particle strength with low number of cells reflects the very high inhomogeneity of forces for such a low number of intercell contacts. The particle may break just as a result of the failure of a single intercell contact. For this reason, the average values in this range for 10 independent simulations do not represent statistically well-defined averages.

In order to evaluate the effect of the degree of disorder in cell configurations, we used particles composed of 150 cells and an increasing degree of disorder $\lambda$. Figure 9 displays the normalized strength as a function of $\lambda$. We see that, as $\lambda$ increases from zero, the particle strength rapidly declines. The particle strength is nearly constant beyond $\lambda = 0.2$. The transition between these two limits seems to be nonlinear. This variation can be explained by remarking that ordered cell structures are formed for $\lambda$ close to zero where the cells have nearly the same size. Such structures have less variability in the orientations of cell contacts and are thus able to sustain large external loads through column-like arrangements of cells. A degree of disorder $\lambda = 0.25$ was used in the simulations reported below.

### 3.3 Effect of intercell strength parameters

Since the stresses and forces inside the particle scale with the applied force, it is generally expected that the particle strength is a linear function of the tensile strength $C_n$ of intercell contacts. However, we expect the shear strength $C_t$ to play a crucial role since an intercell contact fails at this threshold (when sliding occurs) and both $C_n$ and $C_t$ vanish upon failure. Generally, the shear strength $C_t$ is a function of $C_n$ depending on the material [10,11,55]. However, in view of exploring the respective roles of $C_t$ and $C_n$, we varied these parameters independently in the range between 0.25 and 8 MPa.

Figure 10 shows the evolution of the particle strength $\sigma_c$ as a function of $C_n$ for different values of $C_t$. Each data point is an average over 10 independent simulations. We observe

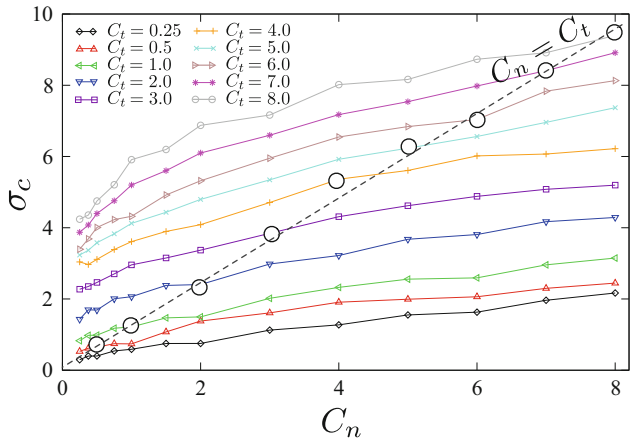


**Fig. 10** Evolution of particle strength as a function of intercell tensile strength $C_n$ for different values of intercell shear strength $C_t$. All stresses are in MPa. The *circles* indicate the data points for $C_n = C_t$

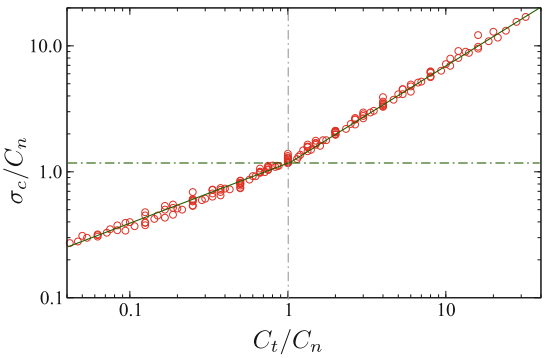


**Fig. 11** Evolution of particle strength normalized by the tensile intercell strength as a function of the ratio of intercell shear to tensile strength. The *solid lines* are power-law fits to the data

a nonlinear dependence of the particle strength on both cell strength parameters. At low values of $C_n$, $\sigma_c$ is rather low but it varies by a factor of 20 as $C_t$ increases to its largest value. At largest values of $C_n$, on the other hand, $\sigma_c$ can take values as much as two times larger but varies by only a factor of 4 as $C_t$ increases in the same range. This shows that the effect of $C_t$ directly depends on the value of $C_n$. In the same figure, we also see that the particle strength for $C_n = C_t$ increases nearly linearly with the latter with a proportionality coefficient of 1.25.

The nonlinear trends observed in Fig. 10 are clearly a consequence of the variation of failure mode in response to the relative values of $C_t$ and $C_n$. In particular, we expect that at low values of $C_t$ with respect to $C_n$, particle breakage by intercell slip requires less energy dissipation and is thus more likely to occur, whereas at high values of $C_t$ with regard to $C_n$, failure by tensile rupture should prevail. This picture is consistent with the evolution of the normalized particle strength $\sigma_c/C_n$ as a function of the ratio $C_t/C_n$ plotted in Fig. 11. First, we see that all data points from simulations nicely collapse on a single curve. Secondly, the data are well fitted by two straight lines of slopes $\alpha$ and $\beta$ representing power laws with exponents $\alpha$ and $\beta$ for $C_t < C_n$ and $C_t > C_n$, respectively, over nearly three decades. Hence, to a good approximation, we have

$$\frac{\sigma_c}{C_n} = 1.25 \times \begin{cases} \left(\frac{C_t}{C_n}\right)^{\alpha} & C_t \le C_n \\ \left(\frac{C_t}{C_n}\right)^{\beta} & C_t > C_n \end{cases}, \tag{10}$$

where $\alpha \simeq 0.5$ and $\beta \simeq 0.8$. Note how these two relations are reduced to a linear function of $C_n$ for $C_t/C_n = 1$ with the same prefactor 1.25 as in Fig. 10.

Equation (10) with the values of the exponents $\alpha$ and $\beta$ can be written as $\sigma_c = 1.25\sqrt{C_n C_t}$ in the range $C_t \le C_n$. This form is a generalization of the observed linear relation in the case $C_n = C_t$. In the range $C_t > C_n$, we have $\sigma_c \simeq 1.25 C_n^{0.2} C_t^{0.8}$. This relation implies that the particle strength increases faster here with $C_t$ than with $C_n$. The exponent $\beta$ is so close to 1 that, in practice, $\sigma_c$ varies almost linearly in response to $C_t$. This seems to contrast the expected picture that in this regime, where $C_t$ is above $C_n$, tensile debonding is more likely to occur, implying thus that the particle strength should be mainly controlled by $C_n$. But the larger values of the intercell shear strength compared to tensile strength is a special condition in which the number of possible configurations accommodating cell motions, and hence failure, declines as $C_t$ increases. In other words, tensile forces are activated to a lower extent since force balance over cells is increasingly ensured by shear forces. Most of time, a mechanically compatible displacement field of the cells at incipient failure involves both tensile debonding and slip at a subset of intercell contacts. This is very similar to the effect of friction in granular materials. Extensive simulations indicate that in packings of polyhedral particles, the friction force mobilization and its anisotropy play a much more important role for the shear strength than in a packing of spherical particles [7]. This effect is reminiscent of "frictional interlocking" in analogy to "geometrical interlocking" of strongly nonconvex particles [26]. The values of the exponents in the above two regimes reflect thus the discrete texture of the particle, steric exclusions between rigid cells and frictional interlocking.

### 3.4 Strength variability

The foregoing analysis of particle strength as a function of intercell strength refers to the measured average values of the particle strength for several independent cell configurations. However, particle-to-particle fluctuations occur to a large extent, and the particle can survive under compressive stresses above its mean strength. As in rocks and agglomerates of fine particles, such fluctuations reflect the presence

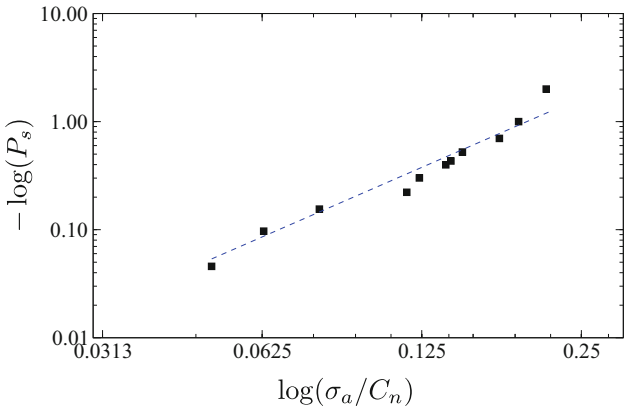


**Fig. 12** Survival probability of particles as function of the mean applied stress for particles composed of 150 cells

and distribution of defects and stress concentration factors, which vary with particle size and/or the size of defects compared to particle size [32,40]. In our simulations, the particle size is kept constant and the number $n_{\mathrm{cl}}$ of cells is varied in a limited range such that our largest spheres contain only 250 cells. This is too small to allow for a systematic analysis of size effect as the particle size increases (except for particles containing below 75 cells and showing slightly lower strength as discussed in Sect. 3.2). For this reason, we focus here on strength variability only for particles composed of 150 cells.

Figure 12 shows the survival probability $P_s$ (the probability that the particle does not break under a load $\sigma_a$) of normalized particle stress $\sigma_a/C_n$ in the case $C_n = C_t$. The log–log plot is consistent with Weibull probability distribution:

$$P_s(\sigma_a/C_n) = e^{-(\sigma_a/\sigma_0)^m}, \tag{11}$$

where $\sigma_0 = kC_n$ is a scaling stress parameter and $m$ is the Weibull modulus. Here, we have $m \simeq 2$, which corresponds to a Gaussian distribution around the mean strength $\sigma_c$, and $k \simeq 1.4$. This is below experimental values, which typically vary in the range from 3 to 10 [24,29,32]. But $m$ is expected to increase with disorder parameter $\lambda$ and particle size [40]. This value of $m$ is an interesting observation since it shows that normal fluctuations should be expected in this range of the rather small numbers of cells.

## 4 Summary and perspectives

In this paper, a three-dimensional model for grain crushing was proposed in the framework of the Contact Dynamics Method. This model belongs to the class of bonding methods as each particle is discretized into a collection of polyhedral cells. The bonding strength between fragments was assumed to obey Tresca's failure criterion. Specifically, the bonding strength is controlled by critical stresses along normal and shear directions between cells. The cells were generated by means of a three-dimensional Voronoi meshing in which the control parameters are the number of cells and their degree of disorder.

A systematic study was undertaken to analyze the effect of various parameters on the particle strength defined as the compressive strength of the particle under diametral loading between two platens. For this purpose, particles of icosahedral shape were loaded between two platens. We showed that particle strength increases with the number of cells and levels off at around 1.25 times the tensile intercell strength. On the other hand, as disorder increases, the particle strength rapidly declines to a well-defined value. The particle strength in those asymptotic states was shown to define two distinct regimes as a function of the ratio of intercell shear strength to tensile strength. In both regimes, the particle strength varies as a power law of both shear and normal intercell strengths. We argued that this nonlinear behavior is a consequence of the evolution of failure modes at the cell scale as the above ratio increases. In particular, the particle strength depends not only on the intercell tensile strength but also crucially on the intercell shear strength, which prevails when the strength ratio is above 1, and amplifies interlocking effect between cells. Finally, we also showed that particle strength fluctuations are consistent with Weibull statistics.

Our bonded-cell model in 3D and its behavior analyzed here under diametral loading provide the first applications of this model in the framework of the contact dynamics method with particles and cells treated as perfectly rigid bodies. This model is simple and capable of reproducing the angular shapes of fragments while conserving the total volume. Further analyses are underway to highlight the initiation of particle failure at the cell scale, the effects of cell disorder on strength variability, and finite size effect as the number of cells is increased. This method can be applied to simulate large samples of crushable particles in 3D.

**Acknowledgments** This work was financially supported by a research grant awarded by the French Alternative Energies and Atomic Energy Commission (CEA). Farhang Radjai would also like to acknowledge the support of the ICoME2 Labex (ANR-11-LABX-0053) and the A*MIDEX projects (ANR-11-IDEX-0001-02) cofunded by the French program Investissements d'Avenir, managed by the French National Research Agency (ANR).

## References

1. Åström J, Herrmann H (1998) Fragmentation of grains in a two-dimensional packing. Eur Phys J B 5(3):551–554
2. Azéma E, Radjai F (2010) Stress-strain behavior and geometrical properties of packings of elongated particles. Phys Rev E 81:051,304

3. Azéma E, Estrada N, Radjai F (2012) Nonlinear effects of particle shape angularity in sheared granular media. Phys Rev E 86:041,301
4. Azéma E, Radjai F (2012) Force chains and contact network topology in sheared packings of elongated particles. Phys Rev E 85:031,303
5. Azéma E, Radjai F, Peyroux R, Saussine G (2007) Force transmission in a packing of pentagonal particles. Phys Rev E 76(1 Pt 1):011,301
6. Azéma E, Radjai F, Saint-Cyr B, Delenne JY, Sornay P (2013) Rheology of 3D packings of aggregates: microstructure and effects of nonconvexity. Phys Rev E 87:052,205
7. Azéma E, Radjai F, Saussine G (2009) Quasistatic rheology, force transmission and fabric properties of a packing of irregular polyhedral particles. Mech Mater 41:721–741
8. Bagherzadeh Kh A, Mirghasemi A, Mohammadi S (2011) Numerical simulation of particle breakage of angular particles using combined dem and fem. Powder Technol 205(1–3):15–29
9. Bandini V, Coop MR (2011) The influence of particle breakage on the location of the critical state line of sands. Soils Found 51(4):591–600
10. Barton N (1976) The shear strength of rock and rock joints. Int J Rock Mech Min Sci Geomech Abstr 13(9):255–279
11. Barton N (2013) Shear strength criteria for rock, rock joints, rockfill and rock masses: Problems and some solutions. J Rock Mech Geotech Eng 5(4):249–261
12. Bratberg I, Radjai F, Hansen A (2002) Dynamic rearrangements and packing regimes in randomly deposited two-dimensional granular beds. Phys Rev E 66(3):1–34
13. Cecconi M, DeSimone A, Tamagnini C, Viggiani G (2002) A constitutive model for granular materials with grain crushing and its application to a pyroclastic soil. Int J Numer Anal Meth Geomech 26(15):1531–1560
14. Chau K, Wei X (1998) Spherically isotropic elastic spheres subject to diametral point load strength test. Int J Solids Struct 25
15. Cheng YP, Nakata Y, Bolton MD (2008) Micro- and macro-mechanical behaviour of dem crushable materials. Géotechnique 58(6):471–480
16. Ciantia M, Arroyo M, Calvetti F, Gens A (2015) An approach to enhance efficiency of dem modelling of soils with crushable grains. Geotechnique 65(2):91–110
17. Cundall PA (1988) Formulation of a three-dimensional distinct element model-Part I. A scheme to detect and represent contacts in a system composed of many polyhedral blocks. Int J Rock Mech Min Sci 25(3):107–116
18. Du Q, Faber V, Gunzburger M (1999) Centroidal Voronoi tessellations: applications and algorithms. SIAM J Numer Anal 41(4):637–676
19. Estrada N, Azéma E, Radjai F, Taboada A (2011) Identification of rolling resistance as a shape parameter in sheared granular media. Phys Rev E 84(1):011306
20. Dubois F, Jean M, et al (2016) LMGC90 wiki page. https://git-xen.lmgc.univ-montp2.fr/lmgc90/lmgc90_user/wikis/home. Accessed 7 Mar 2016
21. Fukumoto T (1992) Particle breakage characteristics of granular soils. Soils Found 32(1):26–40
22. Galindo-Torres S, Pedroso D, Williams D, Li L (2012) Breaking processes in three-dimensional bonded granular materials with general shapes. Comput Phys Commun 183(2):266–277
23. Guimaraes M, Valdes J, Palomino AM, Santamarina J (2007) Aggregate production: Fines generation during rock crushing. Int J Miner Process 81(4):237–247
24. Hardin BO (1985) Crushing of soil particles. J Geotech Eng 111(10):1177–1192
25. Hégron L, Sornay P, Favretto-Cristini N (2014) Compaction of a bed of fragmentable UO2 particles and associated acoustic emission. IEEE Trans Nucl Sci 61(4):2175–2181
26. Jaeger H (2015) Celebrating soft matter's 10th anniversary: Toward jamming by design. Soft Matter 11:12
27. Jean M (1999) The non-smooth contact dynamics method. Comput Methods Appl Mech Eng 177(3–4):235–257
28. Kun F, Herrmann H (1996) A study of fragmentation processes using a discrete element method. Comput Methods Appl Mech Eng 7825(96)
29. Lade PV, Yamamuro J, Bopp P (1997) Significance of particle crushing in granular materials. J Geotech Geoenviron Eng 123(9):889–890
30. Lobo-guerrero S, Vallejo LE (2005) Discrete element method evaluation of granular crushing under direct shear test conditions. J Geotech Geoenviron Eng 131(10):1295–1300
31. Ma G, Zhou W, Chang XL (2014) Modeling the particle breakage of rockfill materials with the cohesive crack model. Comput Geotech 61:132–143
32. McDowell G, Bolton M (1998) On the micromechanics of crushable aggregates. Géotechnique 48(5):667–679
33. McDowell G, Bolton M, Robertson D (1996) The fractal crushing of granular materials. J Mech Phys Solids 44(12):2079–2101
34. Miura N, Murata H, Yasufuku N (1984) Stress-strain characteristics of sand in a particle-crushing region. Soils Found 24(1):77–89
35. Moreau J (1994) Some numerical methods in multibody dynamics: application to granular. Eur J Mech A Solids 13:93–114
36. Nezamabadi S, Radjai F, Averseng J, Delenne J (2015) Implicit frictional-contact model for soft particle systems. J Mech Phys Solids 83:72–87
37. Nezami EG, Hashash YMA, Zhao D, Ghaboussi J (2004) A fast contact detection algorithm for 3-D discrete element method. Comput Geotech 31(7):575–587
38. Nezami EG, Hashash YMA, Zhao D, Ghaboussi J (2006) Shortest link method for contact detection in discrete element method. Int J Numer Anal Meth Geomech 30(8):783–801
39. Nguyen DH, Azéma E, Radjai F (2015) Evolution of particle size distributions in crushable granular materials. Geomechanics from Micro to Macro (Md), pp 275–280
40. Nguyen DH, Azéma E, Sornay P, Radjai F (2015) Bonded-cell model for particle fracture. Phys Rev E 91(2):022,203
41. Nouguier C, Bohatier C, Moreau JJ, Radjai F (2000) Force fluctuations in a pushed granular material. Granular Matter 2:171–178
42. Okabe A, Boots B, Sugihara K, Chiu SN (1992) Spatial tessellations: concepts and applications of voronoi diagrams. Wiley, New York
43. Quey R, Dawson P, Barbe F (2011) Large-scale 3D random polycrystals for the finite element method: Generation, meshing and remeshing. Comput Methods Appl Mech Eng 200(17–20):1729–1745
44. Quezada JC, Breul P, Saussine G, Radjai F (2012) Stability, deformation, and variability of granular fills composed of polyhedral particles. Phys Rev E 86(3):1–11
45. Radjai F, Richefeu V, Jean Mm, Moreau JJ, Roux S (1996) Force Distributions in Dense Two-Dimensional Granular Systems. Phys Rev Lett 77(2):274–277
46. Radjai F, Richefeu V (2009) Contact dynamics as a nonsmooth discrete element method. Mech Mater 41(6):715–728
47. Radjai F, Dubois F (2011) Discrete-element modeling of granular materials. ISTE Ltd and Wiley, London
48. Renouf M, Dubois F, Alart P (2004) A parallel version of the non smooth contact dynamics algorithm applied to the simulation of granular media. J Comput Appl Math 168(1–2):375–382
49. Ries A, Wolf DE, Unger T (2007) Shear zones in granular media: Three-dimensional contact dynamics simulation. Phys Rev E 76(5):1–9
50. Russell AR, Muir Wood D, Kikumoto M (2009) Crushing of particles in idealised granular assemblies. J Mech Phys Solids 57(8):1293–1313

51. Saussine G, Cholet C, Gautier PE, Dubois F, Bohatier C, Moreau JJ (2011) Modelling ballast behaviour under dynamic loading. Part 1: A 2D polygonal discrete element method approach. Comput Methods Appl Mech Eng 195(19–22):2841–2859
52. Saint-Cyr B, Delenne J, Voivret C, Radjai F, Sornay P (2011) Rheology of granular materials composed of nonconvex particles. Phys Rev E 84(4):041302
53. Staron L, Radjai F, Vilotte J (2005) Multi-scale analysis of the stress state in a granular slope in transition to failure. Eur. Phys. J. E 18:311–320
54. Staron L, Vilotte JP, Radjai F (2002) Preavalanche instabilities in a granular pile. Phys Rev Lett 89(1):204,302
55. Stoller RE, Zinkle SJ (2000) On the relationship between uniaxial yield strength and resolved shear stress in polycrystalline materials. J Nucl Mater 283–287(PART I):349–352
56. Taboada A, Chang KJ, Radjai F, Bouchette F (2005) Rheology, force transmission, and shear instabilities in frictional granular media from biaxial numerical tests using the contact dynamics method. J Geophys Res B 110(9):1–24
57. Topin V, Monerie Y, Perales F, Radjai F (2012) Collapse dynamics and runout of dense granular materials in a fluid. Phys Rev Lett 109(18):1–5
58. Tsoungui O, Vallet D, Charmet JC (1999) Numerical model of crushing of grains inside two-dimensional granular materials. Powder Technol 105(1–3):190–198
59. Moreau JJ (1997) Numerical investigation of shear zones in granular materials. In: Wolf D, Grassberger P (eds) Friction, arching, contact dynamics. World Scientific, Singapore
60. Wu S, Chau K (2006) Dynamic response of an elastic sphere under diametral impacts. Mech Mater 38:1039–1060
61. Zhou W, Yang L, Ma G, Chang X, Cheng Y, Li D (2015) Macro-micro responses of crushable granular materials in simulated true triaxial tests. Granular Matter 17(4):497–509
62. Zubelewicz A, Bažant ZP (1987) Interface element modeling of fracture in aggregate composites. J Eng Mech 113(11):1619–1629